TREND

Trapped Radiation Environment Model Development

Time Dependent Radiation-Belt Space Weather Modelling

ESA/TOS-EMA Contract No. 11711/95/NL/JG - CCN 1 to Work Order No. 3

Technical Note 1E/1F

STRV/REM measurements: correlation with the driving parameters and comparison with Salammbô simulations

P. Bühler and M. Kruglanski

(November 1999)

B.I.R.A. – I.A.S.B.	D.E.R.T.S.	P.S.I.
Avenue Circulaire 3 B-1180 Brussel Belgium	ONERA CERT BP 4025 F-31055 Toulouse cedex 4 France	Laboratory for Astrophysics CH-5232 Villigen Switzerland

ESA Technical Management: E.J. Daly (WMA)

To appear in the *SREW Proceedings*, 2000.

Geomagnetic and solar wind parameters to predict the relativistic electron fluxes in the outer radiation belt

Paul Bühler, Laurent Desorgher, Alex Zehnder,
Paul Scherrer Institute, Laboratory for Astrophysics, 5232 Villigen, PSI, Switzerland

Michel Kruglanski, Bart Quaghebeur
Belgian Institute for Space Aeronomy, 1180 Brussels, Belgium

Eamonn Daly
ESTEC, NL-2200 AG Noordwijk, The Netherlands

Abstract

The relativistic electron fluxes of the outer radiation belt are subject to strong temporal variations. In order to find a simple model describing these variations we studied the linear correlation with various geomagnetic and solar wind parameters as function of the magnetic L-shell and the length of period over which the parameters were averaged. We find that the average time giving the best correlation is a function of L and typically around 20 days at $L = 4.5\ R_E$, decreasing to around 5 days at $L = 6.6\ R_E$. In the heart of the belt AP gives the best correlations whereas at Geostationary Orbit best correlations are found with the solar wind speed. Corrections for Dst effect, semiannual modulation of the solar wind - magnetosphere coupling and linear combinations of parameters were tested to improve the correlation coefficients. Best fitting models use a linear combination of eighteen day averaged AP and three day averaged solar wind speed and include a correction for Dst effect.

1. Introduction

The energetic electrons trapped in the earth outer radiation belt form a particular hazard to spacecrafts. Whereas the lower energetic electrons are stopped in the surface material of a satellite and cause surface charging, the higher energetic particles can penetrate and lead to internal charging. The following discharging then can cause damage in sensitive devices [*Wrenn and Smith,* 1996]. In addition the accumulated radiation dose leads to a continuous degradation of instrument performance.

One of the characteristics of the trapped relativistic electron population is its dynamism. The observed fluxes vary on various time scales, from fractions of a day to the solar cycle period, over several orders of magnitude. The variations are driven by the solar wind and interplanetary magnetic field, IMF [*Paulikas and Blake,* 1979]. However, the detailed mechanism is not fully understood yet and subject of active debate [*Blake et al.,* 1997; *Baker et al.,* 1998; *Li et al.,* 1999]

The NASA model AE8 [*Vette,* 1991], which was build with data from the 1960/70 is still used as the quasi standard for the characterization of the space environment. There are two versions, one for solar minimum and one for solar maximum conditions. But each of these models is static. They are supposed to predict long-term averages and can not account for the short-term variations.

In order to improve the situation attempts have been made to use the solar wind, IMF, and geomagnetic indices to describe the electron flux variations. Most of the studies have been focused on the Geostationary Orbit, GEO because of the availability of long term electron data sets at this orbit [*Nagai,* 1988; *Baker et al.,* 1990; *Koons et al.,* 1994]. Data from the CRRES satellite in a geostationary transfer orbit, GTO were used to build a number of models for the entire outer radiation belt zone under different geomagnetic activity conditions which are known as CRRESELE models [*Brautigam and Bell,* 1995]. As sorting parameter, AP_{15} was used, the fifteen day average of AP and it shows that generally the model fluxes increase over the entire outer belt with AP_{15}. In these models the same dependence on AP_{15} is used for all L-values.

We used data from the Radiation Environment Monitor, REM [*Bühler et al.,* 1996] aboard the UK-satellite Strv-1b to investigate possible improvements of the scheme applied for the CRRES data. Strv-1b was launched in June 1994 and was operated until September 1998. It was in a GTO with 7° inclination, thus an orbit similar to CRRES. In this paper we especially address the questions

1. is AP the best sorting parameter ?
2. is 15 days the optimum average time ?
3. does one need to use different sorting parameters/average times at different L-values?

2. Method and data

In order to address these questions we calculated linear correlation coefficients between the logarithm of the 1 MeV electron fluxes, $log(f_e(t,L))$ and different averages of various geomagnetic/solar-wind parameters. The periods over which the parameters were averaged are defined by a lag time t_{lag} and an average time t_{avg} (see figure 1). We investigated the correlation as function of t_{avg} and L. t_{lag} was kept fixed at the value of 1 day. In the following a parameter $\mathcal{P}$, averaged over t_{avg} days with a lag of 1 day is denoted by $\mathcal{P}_{t_{avg},1}(t)$.

figure 1

$$\mathcal{P}_{t_{avg},1}(t) = \overline{\mathcal{P}(\tau)}\Big|_{\tau \geq (t-t_{avg}-1day)}^{\tau \leq (t-1day)} \qquad (1)$$

The correlation coefficient between $log(f_e(t,L))$ and $\mathcal{P}_{t_{avg},1}(t)$ is denoted by $cc_{\mathcal{P}}(L,t_{avg})$.

2.1. Data

We used 1 MeV electron data measured with REM during 1995, different geomagnetic indices from NGDC [*NGDC*], and solar wind and interplanetary geomagnetic field data from instruments aboard the WIND satellite [*WIND*]. The left most column in table 1 contains the investigated parameters. Most of them which contain solar wind and IMF measurements are cited in *Gonzales et al.* [1994] which contains a summary of solar wind - magnetosphere coupling functions used in the past for different purposes. Detailed references are given there.

table 1

In figure 2 the REM 1 MeV electron fluxes at a) $L = 4.5$ and b) $L = 6.6\ R_E$ are plotted versus time for 1995. The time series are characterized by repeated enhancements and decays. Although the maxima and minima at both locations occur closely simultaneously there are significant differences between the two curves. At $L = 6.6\ R_E$ the relative flux variations

figure 2

are larger than at $L = 4.5\ R_E$ and the characteristic timescales, especially the decay times, are obviously shorter. The plotted curves suggest, that there is indeed an L-dependence of the temporal variations and that an average of 15 days may not be optimum at all L-values. This is further supported by the fact, that $cc_{AP}(4.5, 15)$ is 0.74, whereas $cc_{AP}(6.6, 15)$ is only 0.32.

3. Correlations

For each of the parameters listed in table 2 we calculated $cc_{\mathcal{P}}$ for a number of L-bins and t_{avg} values. As an example we show in figure 3 the resulting L-t_{avg}-map of cc_{AP} and $cc_{V_{sw}}$. Panels a) and c) show grayscale maps of the correlation coefficients as function of L and t_{avg}. The black dots mark the positions where for a given L-bin the correlation coefficient is maximum. The subpanels below show the correlation coefficient at these positions as function of L.

The observed L-dependence of $t_{avg,AP,best}$ and $t_{avg,V_{sw},best}$ is typical for most of the investigated parameters. Above $L \approx 5\ R_E$ the best fitting average time is around 3 to 5 days and increases below this limit with decreasing L.

In panels b) and d) of figure 3 the t_{avg}-dependence of the correlation coefficients with $AP_{t_{avg},1}$ and $(V_{sw})_{t_{avg},1}$ at $L = 4.5$ (diamonds) and 6.6 R_E (asterisks) are shown. Whereas at $L = 4.5\ R_E$ the correlation coefficient has a broad maximum around 15 to 20 days, there are two humps at $L = 6.6\ R_E$, one centered around 3 to 5 days and one around 20 days. Also this behaviour is typical for most of the investigated parameters.

For each parameter and L-bin we determined the average time $t_{avg,\mathcal{P},best}(L)$ which yields the higest correlation coefficient $cc_{\mathcal{P},best}(L) = cc_{\mathcal{P}}(L, t_{avg,\mathcal{P},best}(L))$. The $t_{avg,\mathcal{P},best}$ and corresponding $cc_{\mathcal{P},best}(L)$ at $L =$ 4.5 and 6.6 R_E are listed in table 1. There are several points to note:

- At $L = 4.5\ R_E$ the best correlation is found with $AP_{18,1}$. However, the maximum in the correlation versus t_{avg} curve is broad and practically flat between 15 and 20 days. $AP_{15,1}$, as used for the CRRESELE models seems to be a good sorting parameter in the heart of the radiation belt.
- At $L = 6.6\ R_E$ the best correlation is found with $(V_{sw})_{3,1}$. The maximum in the correlation versus t_{avg} curve is rather sharp and peaks at 3 days. $(V_{sw})_{3,1}$ gives here a significantly better correlation than $AP_{15,1}$.
- The averaging time, for which the correlation is maximum, is a function of L. Typically $t_{avg,best}$ is small (few days) at large L and increases below $L \approx 5.0\ R_E$. Exceptions are $V_{sw}B_{imf,z}$, $V_{sw}^2 B_{imf,z}$, and $(\rho V_{sw}^2)^{-1/3} V_{sw} B_{imf,t}^2 sin^4(\Theta/2)$, for which anyhow the correlations are poor at all (L,t_{avg})-values.
- At $L = 6.6\ R_E$ the correlation coefficient versus t_{avg} curves of AP, V_{sw}, and most of the other parameter functions have secondary peaks around $t_{avg,best}$ + 27 days, indicating the influence of recurrent fast solar wind streams.
- At GEO the correlations of all of the parameter functions have a more or less pronounced secondary peak around 20 days, which is approximately the $t_{avg,best}$ value at $L = 4.5\ R_E$. There seem to be two processes, one with a characteristic time of a few days and which is most prominent at large L-values and one with a characteristic time of around 15 to 20 days. This process is most important at lower L-values but also influences the electron fluxes at higher L.

4. Corrections

In order to improve the correlations we included corrections for the Dst effect and semiannual modulation of the solar wind - magnetosphere coupling and also tested linear combinations of different parameters. There are many possible combinations which could not all be tested. We therefore selected $AP_{18,1}$ and $(V_{sw})_{14,1}$ at $L = 4.5\ R_E$ and $AP_{6,1}$ and $(V_{sw})_{3,1}$ at $L = 6.6\ R_E$ to demonstrate the importance of the different approaches.

4.1. Dst correction

The electron fluxes are influenced by the Dst effect. The magnetic field decrease associated with negative Dst values leads to a deceleration of the electrons and with that to a decrease of the electron fluxes [*McIlwain,* 1966; *Desorgher,* 1999]. In order to take this into account the electron fluxes are multiplied with a factor which is a function of Dst. The tested functions are listed in table 2. Each function has one free parameter, α, which can be fitted to find the best correlation between the corrected electron fluxes and a given geomagnetic/solar wind parameter. The resulting α and corresponding correlation coefficient are

given in table 2. The improvements are most significant at $L = 4.5\ R_E$ and less clear at GEO. The difference between the three tested correction functions is negligible.

4.2. Semiannual modulation

The solar wind - magnetosphere coupling strength is a function of the season [*Desorgher et al.,* 1998; *Baker et al.,* 1999]. It is most efficient during spring and fall (equinoxes) and less efficient during summer and winter (solstices). In order to take this into account the solar wind speed is multiplied with a factor which is a function of the season (see table 2) of the three free parameters A, t_0, ω, and the time t which is measured in days. The free parameters can be fitted to find the best correlation between the electron fluxes and the corrected solar wind speed. At $L = 4.5\ R_E$ the semiannual correction yields a significant improvement of the correlation (from non-corrected 0.61 to corrected 0.76), whereas at $L = 6.6\ R_E$ the improvement is small. Altough the two investigated L-values are not conclusive, the results suggest, that the importance of the semiannual modulation decreases with increasing L (lower value of A and less improvement of the correlation at $L = 6.6\ R_E$ compared to $L = 4.5\ R_E$), in agreement with the result found by *Desorgher et al.* [1998]. The fitted parameter values are compatible with t_0=1995-04-21 and $\omega = 0.5$ years.

The same analysis using AP does not yield reasonable results suggesting the modulation in this case to be negligible. This can be expected, since AP itself is affected by the semiannual modulation of the solar-wind-magnetosphere coupling, thus the modulation is already contained in AP [*Joselyn,* 1995].

At low L-values, where the semiannual correction of the solar wind - magnetosphere coupling is important, AP is the better parameter than V_{sw} and at large L-values, where V_{sw} is the best correlating parameter the semiannual correction is small. Thus the correction for the semiannual modulation can not significantly improve the models.

4.3. Linear combination

In section 3 we noted that the $cc_{\mathcal{P}}$ versus t_{avg} curves (see figure 3) suggest two timescales to be important, one of ≈ 5 days and one of ≈ 20 days. The idea here is to use a linear combination of two parameters representing the two different time scales. As an example we selected $AP_{18,1}$ and $(V_{sw})_{3,1}$, the best fitting parameters at $L = 4.5\ R_E$ and GEO. As shown in table 2, using the linear combination does only little improve the correlation.

4.4. Combined corrections

Dst correction, semiannual correction and linear combination of parameters can be combined. But since semiannual correction and linear combination of parameters does not significantly improve the correlation, the combined corrections give similar results as when applying only a Dst correction. The results shown in table 2 were calculated with the Dst correction function $(1 + \alpha \cdot Dst/100)$. Nevertheless, best correlation is found with linear combination of $AP_{18,1}$ and $(V_{sw})_{3,1}$ including a Dst-correction.

5. Flux models

The results of the linear correlation study can be used to select best sorting parameters for simple flux models. Table 3 contains six models at $L = 4.5\ R_E$ and $L = 6.6\ R_E$, which have been determined by a linear fit between the logarithm of the (corrected) 1 MeV electron fluxes and selected (corrected) parameters.

In figure 4 models 5 & 6 are confronted with the actual measurements. The upper panels show the measured (solid line) and predicted (dotted line) 1 MeV electron fluxes. The lower panels show the relative difference of the logarithm of the fluxes. At $L = 4.5\ R_E$ this difference is within ± 0.2 which means that $f_e^{0.8} \leq f_{model} \leq f_e^{1.2}$. At $L = 6.6\ R_E$ the differences are larger (± 0.4).

The largest differences occur during the fast flux rises and periods during which the electron densities are very low. Since the fluxes increase with a characteristic time scale of a day, the rises are badly described by the $>$ three-day averages. The rises only occur during a small fraction of the time and therefore have little weight in the correlation coefficient, which is dominated by the longer lasting periods of relatively high and decreasing fluxes.

All of the models have problems to describe the periods with very low electron fluxes. This is especially pronounced at $L = 6.6\ R_E$ where the electron fluxes can continue to dicrease when the driving parameter levels out. An additional term to account for losses could be useful. Possible loss mechanisms are steady losses due to pitch angle scattering, losses during the main phase of magnetic storms due to the outward

movement of the trapped particles, or losses from stable trapping due to solar-wind shocks.

6. Conclusions

AP_{15} used by *Brautigam et al.* [1995] to produce the CRRESELE models is indeed a good parameter for sorting the relativistic electron fluxes at the heart of the outer radiation belt. And since the highest electron fluxes are encountered in that region, the models can also be expected to be reliable for estimating the total fluences encountered by a spacecraft in GTO. However, at GEO the timescales of the variations are shorter and using shorter average times and the solar wind velocity instead of AP, gives significantly better correlations.

In this paper we investigated only the 1 MeV electrons. But the variations are also a function of energy and a similar investigation including different energies could be of great interest as input for future modeling efforts.

Acknowledgments. The author would like to thank J. Lemaire for usefull discussions. This work was supported by ESA's Technology Research Program, ESA/TOS-EMA, Space Environments and Effects Major Axis.

References

Baker, D.N., McPherron, R.L., Cayton, T.E., Klebesadel, R.W., Linear prediction filter analysis of relativistic electron properties at 6.6 R_E, *J. Geophys. Res., 95,* 15133, 1990

Baker, D.N., Li, X., Blake, J.B., Kanekal, S., Strong electron acceleration in the earth's magnetosphere, *Adv. Space. Res., 21,* 609, 1998

Baker, D.N., Kanekal, S.G., Pulkinnen, T.I., Blake, J.B., Equinoctial and solstitial averages of magnetospheric relativistic electrons: A strong semiannual modulation, *J. Geophys. Res., 26,* 3193, 1999

Blake, J.B., Baker, D.N., Turner, N., Ogilvie, K.W., Lepping, R.P., Correlation of changes in the outer-zone relativistic-electron population with upstream solar wind and magnetic field measurements, *Geophys. Res. Lett, 24,* 927, 1997.

Bühler, P., Ljungfelt, S., Mchedlishvili, A., Schlumpf, N., Zehnder, A., Adams, L., Daly, E., Nickson, R., Radiation environment monitor, *Nucl. Instr. and Meth. in Phys. Res. A, 368,* 825, 1996.

Brautigam, D.H. and Bell, J.T., CRRESELE Documentation, *Tech. Rep. PL-TR–95-2128,* Phillips Laboratory, Hascom Ait Base, MA 01731-3010, 1995

Desorgher, L., Bühler, P., Zehnder, A., Daly, E., and Adams, L., Outer Radiation belt Variations During 1995, *Adv. Space Res.*, **22**, 83, 1998

Desorgher, L., Variations of the Earth's Outer Radiation Belt, REM Observations between 1995 and 1997 and Simulations of Magnetic Storm Effects, PHD Thesis, University of Bern, Switzerland, 1999

Gonzalez, W.D., Joselyn, J.A., Kamide, Y., Kroehl, H.W., Rostoker, G., Tsurutani, B.T., and Vasyliunas, V.M., *J. Geophys. Res., 99,* 5771, 1994

Joselyn, J.A., Geomagnetic activity forecasting: The state of the art, *Reviews of Geophysics, 33,* 383, 1995

Koons, H.C., Gorney, D.J., and Blake, J.B., Long-Term Variability of Electron Radiation Dose in Geosynchronous Orbit, *J. Spacecraft and Rockets, 31,* 557, 1994

Li, X., Baker, D.N., Temerin, M. et al., Rapid enhancements of relativistic electrons deep in the magnetopshere during May 15, 1997, magnetic storm, *J. Geophys. Res., 104,* 4467, 1999

McIlwain, C.E., Ring current effects on trapped particles, *J. Geophys. Res., 71,* 3623, 1966

Nagai, T., Space weather forecast: Prediction of relativistic electron densities at synchrounous orbit, *Geophys. Res. Lett., 15,* 425, 1988

NGDC, NOAA National Data Centers at http:www.ngdc.noaa.govsegpotfldgeomag.shtml

Paulikas, G.A. and Blake, J.B., Effects of the solar wind on magnetospheric dynamics: energetic electrons at the synchronous orbit, in *Quantitative modeling of magnetospheric processes*, edited by W. P. Olson, Geophysical Monograph Series 21, 181, 1979

WIND, WIND information at http:nssdc.gsfc.nasa.govspaceistpwind.html

Vette, J.I., The AE8 trapped electron model environment., *Tech. Rep. NSSDC WDC-A-R&S, 91-24,* NASA–GSFC, 1991

Wrenn, G. and Smith, R., The ESD threat to GEO satellites: empirical models for observed effects due to both surface and internal charging, *Proc. ESA Symposium on Environment Modelling for Space-based Applications, SP-392,* 121, 1996

P. Bühler, L. Desorgher, A. Zehnder., Laboratory for Astrophysics, Paul Scherrer Institute, 5232 Villigen, PSI, Switzerland (e-mail: paul.buehler@psi.ch; laurent.desorgher@phim.unibe.ch; alex.zehnder@psi.ch)

M. Kruglanski, B. Quaghebeur, Belgian Institute for Space Aeronomy, 1180 Brussels, Belgium (e-mail: michelk@mail.magnet.oma.be; bart.quaghebeur@bira-iasb.oma.be)

E. Daly, ESTEC, NL-2200 AG Noordwijk, The Netherlands (e-mail: eamonn@wm.estec.esa.nl)

Received January 3, 1996; revised February 27, 1996; accepted March 31, 1996.

Figure 1. The period of time, over which the parameters are averaged are defined by a lag time, t_{lag} and length of the period, t_{avg}.

Figure 2. 1 MeV electron fluxes at a) $L = 4.5\ R_E$ and b) $6.6\ R_E$ measured with REM aboard Strv-1b. Compared with $L = 4.5\ R_E$, the relative flux variations at GEO are larger and obviously have a shorter characteristic time scale.

Figure 3. Correlation coefficient cc_{AP} (left panels) and $cc_{V_{sw}}$ (right panels). Panels a) and c) show greyscale coded L-t_{avg}-maps of the correlation coefficients. The black dots mark the positions where the correlation is maximum at a given L-bin. The panels below show the maximum correlation coefficient at a given L-bin as function of L. In panels b) and d) the correlation coefficients at $L = 4.5\ R_E$ (diamonds) and $L = 6.6\ R_E$ (astrisks) are plotted versus t_{avg}.

Figure 4. Flux model results for a) model 5 (see table 3) and b) model 6. In the upper panels the measured (solid line) and predicted (dotted line) 1 MeV electron fluxes are plotted versus time. The lower panels show the relative difference between the logarithms of the measured and predicted fluxes. Model fluxes for which this difference is larger than 0.2 are marked with red, such for which the difference is lower than -0.2, are marked with blue.

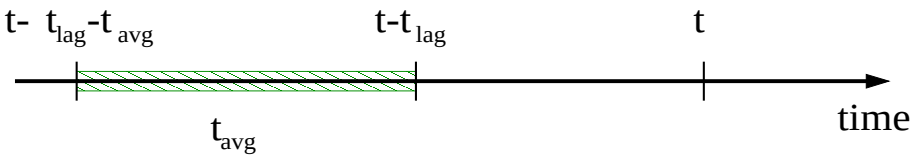

Figure 1.

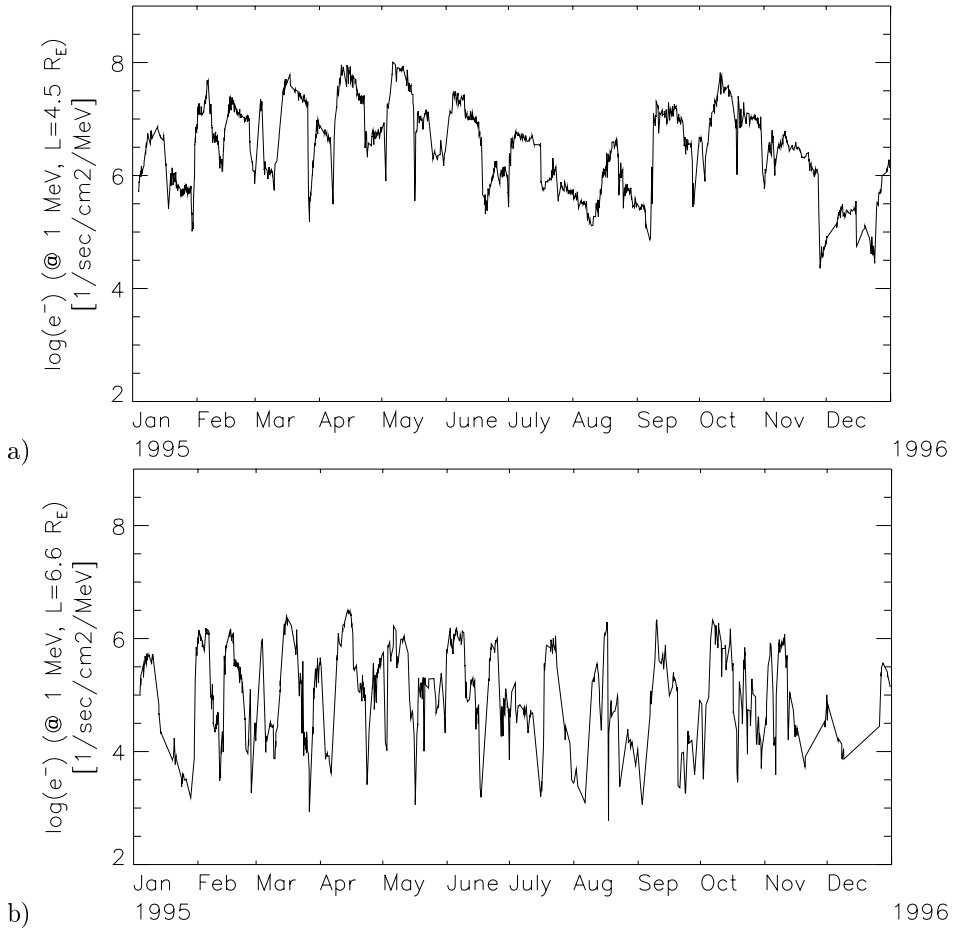
log(e⁻) (@ 1 MeV, L=4.5 R_E)
[1/sec/cm2/MeV]
8
6
4
2
Jan Feb Mar Apr May June July Aug Sep Oct Nov Dec
1995
1996
a)
log(e⁻) (@ 1 MeV, L=6.6 R_E)
[1/sec/cm2/MeV]
8
6
4
2
Jan Feb Mar Apr May June July Aug Sep Oct Nov Dec
1995
1996
b)

Figure 2.

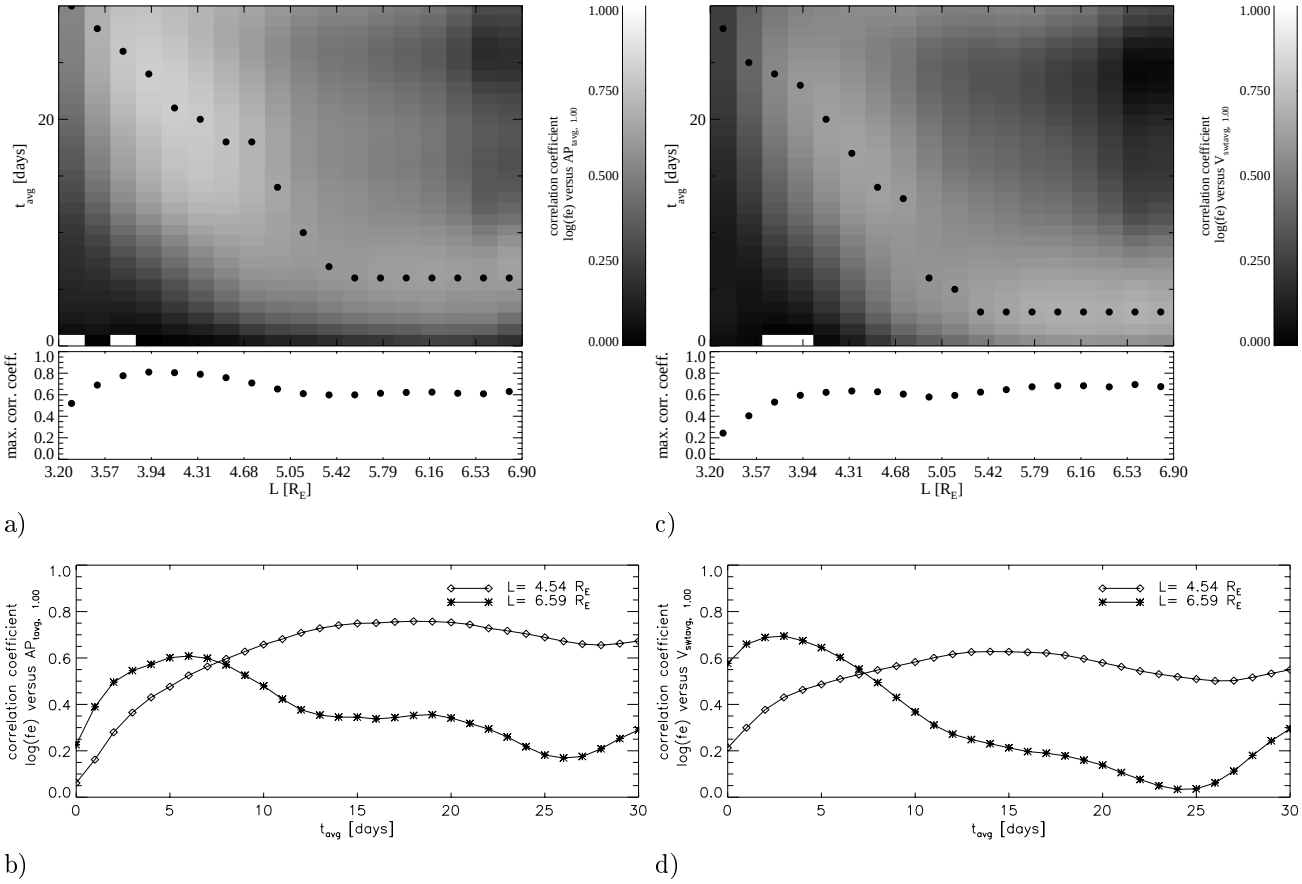
a)
c)
b)
d)
L [R_E]
max. corr. coeff.
t_avg [days]
correlation coefficient
L= 4.54 R_E
L= 6.59 R_E

Figure 3.

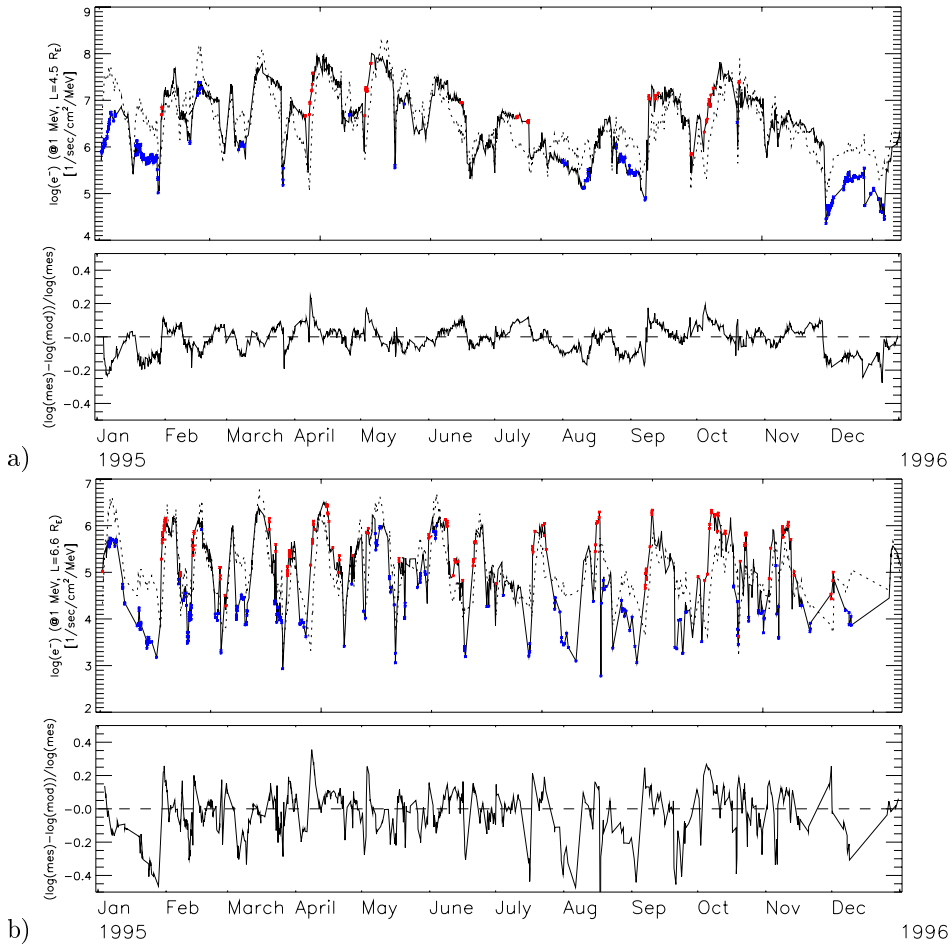
log(e⁻) (@1 MeV, L=4.5 Re) [1/sec/cm²/MeV]
(log(mes)−log(mod))/log(mes)
Jan
Feb
March
April
May
June
July
Aug
Sep
Oct
Nov
Dec
1995
1996
a)
log(e⁻) (@1 MeV, L=6.6 Re) [1/sec/cm²/MeV]
(log(mes)−log(mod))/log(mes)
Jan
Feb
March
April
May
June
July
Aug
Sep
Oct
Nov
Dec
1995
1996
b)

Figure 4.

Table 1. Parameter functions used to study correlation with 1 MeV electron fluxes. The right four columns contain $t_{avg,best}$ and corresponding $cc_{\mathcal{P},best}$ at $L = 4.5\ R_E$ and $L = 6.6\ R_E$ (see text for details).

Function	$t_{avg,best}$ [days]		$cc_{\mathcal{P},best}$	
	4.5 R_E	6.6 R_E	4.5 R_E	6.6 R_E
AP	18	6	0.76	0.61
aa	19	6	0.73	0.61
Dst	18	2	0.68	0.46
V_{sw}	14	3	0.63	0.69
$V_{sw}B_{imf,z}$	6	5	0.26	0.38
$V_{sw}B_{imf,s}$ [(1)]	21	5	0.53	0.33
$V_{sw}B_{imf,t}$ [(2)]	19	8	0.58	0.42
$V_{sw}^2B_{imf,z}$	7	5	0.32	0.36
$V_{sw}^2B_{imf,s}$	20	5	0.64	0.51
$V_{sw}B_{imf,t}sin(\Theta/2)$ [(3)]	20	7	0.59	0.49
$V_{sw}B_{imf,t}sin^2(\Theta/2)$	20	6	0.58	0.50
$V_{sw}B_{imf,t}sin^4(\Theta/2)$	20	6	0.58	0.48
$(\rho V_{sw}^2)^{1/2}V_{sw}B_{imf,z}$	21	5	0.28	0.35
$(\rho V_{sw}^2)^{-1/3}V_{sw}B_{imf,t}^2sin^4(\Theta/2)$	21	22	0.39	0.24
$(\rho V_{sw}^2)^{1/6}V_{sw}B_{imf,t}sin^4(\Theta/2)$	21	7	0.61	0.50
$\epsilon = V_{sw}L_0^2B_{imf}^2sin^4(\Theta/2)$ [(4)]	21	8	0.66	0.52

[(1)] $B_{imf,s} = \begin{cases} B_{imf,z} & : \quad B_{imf,z} > 0 \\ 0 & : \quad B_{imf,z} \leq 0 \end{cases}$

[(2)] $B_{imf,t}^2 = B_{imf,y}^2 + B_{imf,z}^2$

[(3)] Θ is the clock angle between $B_{imf,z}$ and the IMF vector projected at the magnetopause ($[B_{imf,y},\ B_{imf,z}]$)

[(4)] L_0 is a constant scale-length factor, equal to 7 R_E

Table 2. Correction functions, best fitting parameters, and corresponding linear correlation coefficients.

Correction function		correlation coefficient $L = 4.5\ R_E$		$L = 6.6\ R_E$	
No correction		$AP_{18,1}$	$(V_{sw})_{14,1}$	$AP_{6,1}$	$(V_{sw})_{3,1}$
		0.76	**0.61**	**0.63**	**0.69**
Dst correction					
$exp(\alpha \cdot Dst/100)$		**0.83**	**0.73**	**0.64**	**0.72**
	$\alpha =$	-0.209	-0.027	-0.589	-0.290
$1 + \alpha \cdot Dst/100$		**0.83**	**0.74**	**0.64**	**0.72**
	$\alpha =$	-0.225	-0.027	-0.743	-0.337
$(1 + \alpha)^{(-Dst/100)}$		**0.83**	**0.73**	**0.64**	**0.72**
	$\alpha =$	0.233	0.027	0.802	0.336
Semiannual correction					
$1. + A \cdot cos(2\pi(t_0 - t)/\omega)$					
		-	**0.76**	-	**0.70**
	$A =$		0.122		0.056
$t_0 \approx$ 1995-04-21					
$\omega \approx 0.5$ years					
Linear combination					
$\frac{AP_{18,1}}{max(AP_{18,1})} + \beta \cdot \frac{(V_{sw})_{3,1}}{max((V_{sw})_{3,1})}$					
$max(AP_{18,1}) = 22.69$, $max((V_{sw})_{3,1}) = 700.0$					
		0.79		**0.71**	
	$\beta =$	0.176		4.87	
Linear combination with Dst correction					
		0.84		**0.75**	
	$\alpha =$	-0.253		-0.412	
	$\beta =$	0.283		3.67	

Table 3. 1 MeV electron flux models for $L = 4.5\ R_E$ and GEO.

Model		$log10(f_e) =$
1	$L = 4.5\ R_E$	$4.67 + 0.145 \cdot AP_{18,1}$
2	$L = 6.6\ R_E$	$2.52 + 5.73 \cdot 10^{-3} \cdot (V_{sw})_{3,1}$
3	$L = 4.5\ R_E$	$(4.57 + 0.167 \cdot AP_{18,1})/(1 - 2.25 \cdot 10^{-3} \cdot Dst_{0,0})$
4	$L = 6.6\ R_E$	$(2.25 + 6.88 \cdot 10^{-3} \cdot (V_{sw})_{3,1})/(1 - 3.37 \cdot 10^{-3} \cdot Dst_{0,0})$
5	$L = 4.5\ R_E$	$(4.11 + 1.57 \cdot 10^{-1} \cdot (AP_{18,1} + 9.17 \cdot 10^{-3} \cdot (V_{sw})_{3,1}))/(1 - 2.53 \cdot 10^{-3} \cdot Dst_{0,0})$
6	$L = 6.6\ R_E$	$(1.70 + 5.47 \cdot 10^{-2} \cdot (AP_{18,1} + 1.19 \cdot 10^{-1} \cdot (V_{sw})_{3,1}))/(1 - 4.12 \cdot 10^{-3} \cdot Dst_{0,0})$

Confrontation of Salammbô predictions of the storm-time electron belt population to in situ Strv/REM measurements

M. Kruglanski[1], D. Boscher[2], P. Bühler[3] and D. Heynderickx[1]

[1] *Belgian Institute for Space Aeronomy, B-1180 Brussels, Belgium*
[2] *DESP ONERA/CERT, F-31055 Toulouse, France*
[3] *Paul Scherrer Institute, CH-5232 Villigen PSI, Switzerland*

Measurements of the Radiation Environment Monitor aboard the Strv-1b satellite have been confronted with the results of the Salammbô-3D code for the period of time from 5 to 18 April '95. Shortcomings of the current state of the Salammbô model are discussed.

INTRODUCTION

The prediction of the electron radiation belt dynamics during storm periods is an important issue in space weather forecasting. The Radiation Environment Monitor (REM) aboard the Strv-1B satellite in GTO orbit provides a wealth of data for studying the radiation environment and evaluating empirical and theoretical models of the radiation belts. The REM detector [*Bühler et al., 1996*] is composed of two independent shielded silicon diodes measuring the linear energy transfer of charged particles. The shielding consists in each case of a dome of aluminium, but one diode has an additional shielding of tantalum. The combination of the signals from both detectors allows the determination of electron fluxes in three energy bins ranging from 1 to 10 MeV. The typical accumulation time is of the order of 100 seconds.

From June '94 to September '98, the REM instrument was in operation aboard the Strv-1b satellite, launched into a highly elliptical GTO orbit with apogee and perigee altitude of 300 km and 36000 km, respectively, a period of about 10 hours, and inclination of 7 degrees. The orbit passes repeatedly through the Earth radiation belts. The Strv-1b/REM data set [*Bühler et al., 1999*] therefore provides a good coverage of the equatorial part of the radiation belts over a period of four years. Due to the high spin rate of the satellite with respect to the accumulation time and the large opening angle of the detector, only omnidirectional fluxes are obtained from the Strv-1b/REM measurements. Due to the limited data storage capacity aboard Strv-1b, REM was not continuously operated, so that some orbits are missing. Parts of the Strv-1b/REM data have already been analysed in other studies, e.g. by *Bühler et al.* [*1999*], *Desorgher et al.* [*1997, 1998*] and *Daly et al.* [*1999*].

DESP (*Département d'Étude Spatiale*) has developed the Salammbô-3D code [*Beutier and Boscher, 1995*] to simulate the radiation belt dynamics by solving a classical Fokker-Planck diffusion equation in the (M, J, L^*) space as a function of time. In the framework of the ESA/ESTEC TREND contract, Salammbô-3D results have been confronted to in situ data for several magnetic storms during two periods of time for which sufficient data were

available. The first period corresponds to the CRRES mission for which data from the Meteosat-3, GOES-6 and GOES-7 spacecraft are also available. Comparisons between CRRES/MEA measurements [*Vampola et al., 1992*] and Salammbô-3D simulations have been used to include and tune a temporal variation of the radial diffusion coefficients and of the plasmapause location into the Salammbô model. The final results for the four storms studied during this period show good agreement between measurements and simulations [*Boscher and Bourdarie, 1999*].

In order to evaluate the generality of the adaptations, we have applied the code with the same tuning to a second period. The second period corresponds to the conjunction of the Strv-1b, Meteosat-3, GOES-7 and WIND missions and extends from April '94 to December '95.

Four storms occurring during this period were studied. In this paper, we only report on the comparison for the period 5–18 April '95. This period covers a storm associated with a fast solar wind stream, with good data availability from Strv-1b/REM but also from the SEM-2 instrument aboard Meteosat-3, from GOES-7 and from WIND. The GOES and WIND data were not used during the computations but are important for the understanding and interpretation of the results. The Meteosat-3/SEM-2 instrument [*Coates et al., 1991*] provides electron flux measurements in 5 energy channels between 43 and 300 keV at geostationary orbit. The SEM-2 measurements have been used to determine the boundary conditions of the Fokker-Planck equation during the studied period. The Strv-1b/REM data are confronted with Salaambô-3D to evaluate the Salammbô capabilities to reproduce the dynamics of electrons in an energy range higher than the CRRES/MEA range (0.12–1.7 MeV). The Strv-1b data are not use to define the initial condition.

The Salammbô-3D model and its different ingredients used for the simulation are described in the first section. The second section is dedicated to the confrontation between Strv-1b/REM measurements and Salammbô results. The results are not as good as for the CRRES period; possible shortcomings are discussed in the third section. The conclusions are given in the last section.

Figure 1

1. MODELLING THE 7 APRIL STORM

1.1. Description of the Salammbô-3D model

The Salammbô-3D model is the first of a series of numerical codes developed by DESP to study the dynamics of the Earth radiation belts. It is based on the solution of a classical Fokker-Planck diffusion equation in the three adiabatic invariants M, J, L^*: the magnetic moment, the second action integral and Roederer's [*1970*] magnetic shell parameter, respectively. The ingredients needed for such a diffusion model are particle sources, transport and loss processes, and also the initial and boundary conditions.

For electrons, the Salammbô-3D model does not include explicit sources inside the radiation belts. The only source is localised at the boundary $L^* = 7$ of the model, and thus corresponds to storm and substorm injections.

The particle transport is assumed to be due only to Coulomb interaction with neutral atoms or cold electrons, to wave interactions and to electromagnetic fluctuations. The Coulomb interaction occurs with neutrals from the exosphere or cold electrons from the plasmasphere. It is evaluated with the help of an eccentric tilted dipole magnetic field (the coefficients of which are evaluated from the IGRF models), the exosphere neutral model MSIS-86 and the model for plasmaspheric electrons of *Carpenter and Anderson* [*1992*]. The Coulomb interaction is used in Salammbô with yearly averaged parameters to calculate a friction term and pitch angle diffusion coefficients. Wave interactions related to plasmaspheric hiss, whistlers and VLF transmitters are also used to evaluate pitch angle diffusion coefficients. The evaluation of the wave interactions makes use of the *Abel and Thorne* [*1998*] calculations and of a plasmapause location r_p related to the maximum value of K_p in the preceding day by the *Carpenter and Anderson* [*1992*] formula

$$r_p = 5.6 - 0.46\ K_{pmax}. \quad (1)$$

Electromagnetic fluctuations inside the magnetosphere lead to radial diffusion and their classical coefficients. To adapt the radial diffusion to the magnetic activity, the radial diffusion coefficients have been multiplied by the factor

$$g = e^{0.74\ Kp} \quad (2)$$

[*Bourdarie et al., 1996*; *Boscher et al., 1998*].

Most of the losses occur in the loss cone where particles are precipitated mostly by pitch angle diffusion. The loss regions are thus located at the boundaries of the Salammbô model, where the electron fluxes are forced to zero. Internal losses are included as well by taking synchrotron losses into account [*Pugacheva et al., 1998*].

1.2. Application of Salammbô-3D

To apply Salammbô-3D, the conditions at the different boundaries have to be determined. At the inner edge, the electron fluxes were forced to zero to take into account the absorption by the atmosphere. At the outer edge, defined by $L^* = 7$, the electron fluxes were set to measured values based on the Meteosat-3/SEM-2 data provided by MSSL [*Lemaire et al., 1995*]; note that McIlwain's [*1961*] *L* for the Meteosat-3 orbit varies between 6.8 and 7.4 when evaluated with the IGRF 1995 geomagnetic field model and the *Olson and Pfitzer* [*1977*] quiet external magnetic field model. Since Meteosat-3/SEM-2 covers only a limited energy range, the data are extrapolated down to 2.2 keV and up to 600 keV. The energy range is extended below 22 keV with the energy spectrum is obtained from ATS6 measurements [*Parks et al., 1977*]. Above 600 kev, the electron fluxes are forced to zero. Based on CRRES/MEB data [*Gussenhoven et al., 1985*], the pitch angle distribution is fixed at $L^* = 7$ to the power law $\sin^{3.32} \alpha_0$ at all energies. The Meteosat-3/SEM-2 flux data, available with a time

resolution of 500 s, allow to generate highly dynamical boundary conditions.

The energy range and resolution of the Strv-1b/REM data are too limited to set the initial conditions for a Salammbô-3D run. Therefore, the initial conditions from a run for the CRRES period are used (24 September 1991 [*Boscher and Bourdarie, 1999*]).

The Salammbô-3D model is run on a grid of 25×25×25 points in (M, J, L^*) space, with a time step of 34 s. For analysis and presentation purposes, the results are projected on a grid of 9×18×21 points in the (E,α_0, L^*) space, every 3 hours.

2. THE PERIOD 5–18 APRIL '95

The selected 13-day period beginning 5 April 1995 covers a magnetic storm that was initiated by a fast solar wind stream impinging upon the magnetosphere. The solar wind velocity was high and nearly constant during 4 days. The velocity and density of the solar wind for the 13-day period as observed by WIND are displayed on the top panels of Figure 1. After the shock, the GOES-7 data indicates a jump of the energetic $E > 2$ MeV electron flux at geostationary distance above 10^4 $cm^{-2}s^{-1}sr^{-1}$ which is maintained during 7 days (third panel of Figure 1). The electron flux even exceeds 10^5 $cm^{-2}s^{-1}sr^{-1}$, 3 days after the shock. The electron fluxes observed by the five energy channels of Meteosat-3/SEM-2 are also displayed on Figure 1, as well as the Meteosat-3 L values, K_p and D_{st}. The GOES-7 and Meteosat-3 spectra clearly show that at geostationary distance the flux enhancement occurs first at low energies and then at higher energies: the elapsed time between the changes at 50 keV and at 2 MeV is about 2 days.

In Figure 2, the measurements of the Strv-1b/REM instrument are presented for comparison with the results of the Salammbô simulation. The Strv-1b/REM data are ordered according to McIlwain's [*1961*] L evaluated with IGRF 1995 and the *Olson and Pfitzer* [*1977*] quiet model in the same way as the Meteosat-3 data. Except for 6 and 13 April, the Strv-1b/REM data provides a good spatial coverage of the radiation belts. The REM instrument is not capable of separating electrons and protons below $L = 2.5$. During the main phase of the magnetic storm, the electron fluxes are decreasing together with D_{st} everywhere in the outer belt. At the start of the recovery phase, the electron fluxes increase rapidly to higher values than before the storm onset. They continue to increase during the recovery phase, the fluxes continue to increase slowly. The dynamics of both Strv-1b/REM energy channels are very similar. The maximum flux is reached after 5 days at $L = 5.5$, and after 9 days at $L = 4$.

Figure 2

On panels 4 to 6 of Figure 2, unidirectional electron flux maps produced from Salammbô results are displayed: the 600 keV equatorial flux, the $L^* = 4$ equatorial energy spectrum and the $L^* = 4$ pitch angle distribution for 600 keV, respectively. The storm appears clearly with an increase of the electron fluxes during the recovery phase. The Salammbô simulation is thus able to reproduce the basic trend of the magnetic storm. However, the electron

dropout during the main phase of the storm does not seem to be simulated except at high L where it is probably forced by the boundary conditions. Part of this particle dropout can be related to the decrease of the magnetic field when the ring current is enhanced [*Desorgher et al., 1998*] or during the growth phase of substorms [*Sauvaud et al., 1996*].

In order to directly compare the Strv-1b/REM measurements and the Salammbô simulation, the Salammbô results have been integrated in energy and pitch angle to predict the REM measurements along the Strv-1b orbit. The result of the simulation of the 1.0–2.2 MeV Strv-1b/REM channel is presented on panel 7 of Figure 2. The simulated fluxes do not follow the measurements shown on the first panel: there are no significant variations in the Salammbô flux except at the end of the period for the lowest L values. For a more detailed comparison, the Salammbô predictions and Strv-1b/REM measurements are shown in Figure 3 for four Strv-1b orbits: one orbit before the storm, one orbit during the main phase and two orbits during the recovery phase. Before the storm, the measurements and predictions look similar in spite of Salammbô initial conditions being based on data from a different epoch. During the storm, the predicted electron fluxes do not decrease during the growth phase, as already observed on Figure 2, and Salammbô overestimates the REM flux by a factor 10. This can be partly due to the effect of L as the Strv-1b/REM measurements were plotted using a McIlwain L and a static magnetic field while the Salammbô results are obtained in (M, J, L^*) space. During the recovery phase, the differences between measurements and predictions become even more significant. Both measured and simulated fluxes increase in the outer belt region, but the shape, the growth rate and the amplitude are very different. For large L values the discrepancies are probably due to boundary conditions. As noted before, at $L^* = 7$ the fluxes above 600 keV are forced to zero. Moreover, as the electron acceleration is thought to be due to the recirculation process [*Fujimoto and Nishida, 1990*] —a phenomenon that is highly non-linear— comparisons are better for low energies than for higher one. The recirculation is a combined effect of radial and pitch angle diffusion, and neither processes adequately modelled.

Figure 3

3. SHORTCOMINGS OF THE SIMULATION

For the simulation of Strv-1b/REM measurements presented in Figures 2 and 3, the Salammbô-3D model has been applied without any fitting procedure to minimize the discrepancies between measurements and observation, even at the start of the period. The results therefore provide the opportunity to determine the strengths and weaknesses of this type of model in predicting the space environment for space weather applications. The success or failure of a simulation are related to:

- the availability of in situ measurements, especially the boundary conditions;
- the suitability of these data to derive initial and boundary conditions for the model, although the same initial conditions were used with success for different situations (see Figure 3 panel 1);

- the modelisation of the physical processes.

The availability of in situ measurements is probably the most important barrier to good-quality prediction tools. In our case, initial conditions were not available and experimental boundary conditions are limited to almost equatorially mirroring electrons of energies between 43 and 300 keV.

The limited energy range of the data used to determine the boundary conditions also strongly influences the results. Figure 4 shows the energy increases for equatorially mirroring electrons due to radial diffusion from $L^* = 7$. The energies at $L^* = 7$ correspond to the Meteosat-3/SEM energy channels. These particles only reach the energy levels of the Strv-1b/REM detector below $L^* = 4$. Therefore, the $E > 1$ MeV electron population is poorly affected by the magnetic storm in the Salammbô simulation when $L > 5$. This could probably explain a great part of the discrepancies between Salammbô results and Strv-1b/REM observations during the recovery phase.

Figure 4

Another shortcoming, related to the building of the initial and boundary conditions, is the reduction of the experimental data. In addition to the problem of the cross calibration between different experiments, we have also to associate the measurements to L and α_0 values in order to compare those measurements with the Salammbô-3D simulation. In our study, L is evaluated with the help of *McIlwain*'s [*1961*] formula where the Earth's magnetic moment M_0 is fixed to 0.311653 G Re^3, and α_0 is defined as

$$\sin^2 \alpha_0 = M_0 L^{-3} B_m^{-1}, \quad (3)$$

where B_m is the magnetic field intensity at the mirror point. As mentioned previously, the magnetic field model used to order the Strv-1b/REM and Meteosat-3/SEM data is static, i.e. it is not affected by the magnetic storm. On Figure 5, the L values used in our studies are compared to values obtained with the *Pfitzer et al.* [*1988*] dynamic external magnetic field model for both Meteosat-3 and Strv-1b on 7 April 1995. The *Pfitzer et al.* [*1988*] dynamic model depends on D_{st} and solar wind parameters. During the main phase, the differences between both L evaluations exceed one Earth radius for Meteosat-3 as well for Strv-1b. Using a dynamic magnetic field model will clearly affect the comparison between Salammbô results and Strv-1b measurements, especially during the main phase (second panel of Figure 3). But since the dynamic magnetic field model also causes L variation for Meteosat-3, it precludes a continuous determination of the boundary conditions near $L^* = 7$.

Figure 5

The last class of shortcoming is related to the modelisation of the physical processes acting in the magnetosphere. Some model parameters, e.g. the ionosphere high altitude densities, the magnetic and electric field fluctuations, or the wave characteristics, are not known well enough. The most uncertain coefficients are certainly the radial diffusion coefficients, which should depend on magnetic activity. In this simulation, this dependence is implemented only by an ad-hoc exponential on K_p (see Equation 2). The dynamics

of the magnetic field during periods of magnetic activity should also be included in the Salammbô-3D model. During the main phase of a magnetic storm, non-adiabatic modifications of the particle movement and energy occur: particles are subject to strong induced electric fields and can be lost by drifting into the magnetopause [*Desorgher et al., 1998*; *Desorgher, 1999*].

4. CONCLUSIONS

The Salammbô-3D code is a powerful tool to analyse the radiation belt behaviour during high magnetic activity events. For electrons below 1 MeV, most of the physical phenomena occurring in the dynamics of their population seem to be modelled in the code, even if some model aspects have to be improved such as radial diffusion coefficients, wave spectrum and wave localization. The comparison with Strv-1b/REM measurements shows that Salammbô has to be improved in order to correctly simulate populations of very high energetic electrons, especially in the outer belt. In particular, an additional loss mechanism is needed at large L and the dependence of the radial diffusion on magnetic activity has to be enhanced.

The development of tools and models like Salammbô is restrained by the lack of in situ measurements. Continuous measurements on a broad energy spectrum should help to better understand the dynamics in the outer belt and to better identify the model shortcomings. The model development, as well as the comparison between predictions and measurements, is also affected by the way to define the L parameter. Different definitions of L can lead to differences greater than one Earth radius in the evaluation of L. This variation could clearly lead to misinterpretation of comparisons between theoretical models and experimental data.

Acknowledgements. This work was supported by ESA, Space Environments and Effects Major Axis, under ESTEC Contract No. 8011/88/NL/MAC.

REFERENCES

Abel, B., and R. Thorne, Electron scattering loss in Earth's inner magnetosphere 1. Dominant physical processes, J. Geophys. Res. 103, 2385–2396, 1998

Abel, B., and R. Thorne, Electron scattering loss in Earth's inner magnetosphere 2. Sensitivity to model parameters, J. Geophys. Res. 103, 2397–2407, 1998

Beutier T., D. Boscher, and M. France, Salammbô: A three-dimensional simulation of the proton radiation belt, J. Geophys. Res. 100, 14853–14861, 1995.

Boscher, D., and S. Bourdarie, Physical modelling of the outer belt high energy electrons, Workshop on Space Weather, Noordwijk (The Netherlands), 11–13 November 1998, ESTEC WPP-155, 411–414, 1999

Bourdarie, S., D. Boscher, T. Beutier, J. Sauvaud, M. Blanc, and R. Friedel, A physics based model of the radiation belt flux at the day timescale, Symposium on Environment modelling for space-based applications, Noordwijk (The Netherlands), 18–20 September 1996, ESA SP-392, 159–163, 1996

Boscher, D., S. Bourdarie, R. Friedel, and A. Korth, Long term dynamic for low energy protons, Geophys. Res. Lett., 4129, 1998

Bühler, P., S. Ljungfelt, A. Mchedlisshvili, N. Schlumpf, A. Zehnder, L. Adams, E. Daly, and R. Nickson, Radiation environment monitor, Nucl. Instr. and Meth. in Phys. Res. A 368, 825–831, 1996.

Bühler, P., L. Desorgher, A. Zehnder, and E. Daly, Observation of the radiation belts with REM, Workshop on Space Weather, Noordwijk (The Netherlands), 11–13 November 1998, ESTEC WPP-155, 333–337, 1999.

Carpenter, D., and R. Anderson, An ISEE/whistler model of equatorial electron density in the magnetosphere, J. Geophys. Res. 97, 1097–1108, 1992

Coates, A., A. Johnstone, D. Rodgers, and G. Wrenn, Quest for the source of Meteosat anomalies, Proceedings of spacecraft charging technology conference 1989, ed R.C. Olsen, Naval Postgraduate School, Monterey (CA), 120–146, 1991

Daly E., P. Bühler, and M. Kruglanski, Observations of the outer radiation belt with REM and comparisons with models, IEEE Nuclear and Space Radiation Effects Conference, Norfolk, VA, 1999

Desorgher, L., Variations of the Earth's outer electron belt - REM observations between 1995 and 1997 and simulations of magnetic storm effects, Ph.D. thesis, Universität Bern (Switzerland), 1999

Desorgher, L., P. Bühler, A. Zehnder, E. Daly, L. Adams, Outer radiation belt losses during magnetic storm,Workshop Space Radiation Environment Modelling: New Phenomena and Approaches, Moscow (Russia), October 7–9, 1997.

Desorgher, L., P. Bühler, E. Fluckiger, A. Zehnder, E. Daly, L. Adams, Modelling of the outer electron belt during magnetic storms, 32nd COSPAR Scientific Assembly, Nagoya (Japan) 12– 19 July 1998.

Fujimoto, M., and A. Nishida, Energization and anisotropization of energetic electrons in the earth's radiation belts by the recirculation process, J. Geophys. Res. 95, 4265–4270, 1990

Gussenhoven, M., E. Mullen, and R. Sagalyn, CRRES/ SPACERAD Experiment Descriptions, AFGL Tech. Rep. 85-0017, Hanscom AFB (Massachusetts), 1985

Lemaire, J., A. Johnstone, D. Heynderickx, D. Rodgers, S. Szita, and V. Pierrard, Trapped radiation environment model development TREND-2 - final report, Aeronomica Acta 393, 133–184, 1995

McIlwain, C. E., Coordinates for Mapping the Distribution of Magnetically Trapped Particles, J. Geophys. Res., 66, pp. 3681–3691, 1961.

Olson, W. P., and K. A. Pfitzer, Magnetospheric magnetic field modeling, Annual Scientific Report, AFOSR Contract No. F44620-75-C-0033, 1977.

Parks, G., C. Lin, B. Mauk, S. DeForest, and C. McIlwain, Characteristics of magnetospheric particle injection deduced from events observed on August 18, 1974, J. Geophys. Res. 82, 5208–5214, 1977

Pfitzer, K. A., W. P. Olson, and T. Mogstad, A time dependent source driven magnetospheric magnetic field model, EOS, 69, 426, 1988.

Pugacheva G., A. Gusev, I. Martin, D. Boscher, S. Bourdarie, and W. Spjeldvik, Numerical modeling of magnetospheric electron radial transport with accounting synchrotron radiation losses, Geophys. Res. Lett. 25, 1519–1522, 1998.

Roedere, J., Dynamics of geomagnetically trapped radiation, Springer-Verlag, New York, 106–111, 1970

Sauvaud, J., T. Beutier, and D. Delcourt, On the origin of flux dropouts near geosynchronous orbit during the growth phase of substorms 1. Betatron effects, J. Geophys. Res. 101, 19911–19919, 1996

Vampola, A., J. Osborn, and B. Johnson, The CRRES magnetic electron spectrometer, J. Spacecraft and Rockets 29, 592–594, 1992

CAPTIONS

Figure 1. For the period from 5 to 18 April 1995, from top to bottom, the solar wind bulk velocity and density from WIND, the GOES-7 $E > 2$ MeV electron flux, the geostationary electron spectrum from Metosat-3/SEM-2 and corresponding McIlwain's L, the K_p planetary index and the D_{st} magnetic activity index.

Figure 1. For the period from 5 to 18 April 1995, from top to bottom, the solar wind bulk velocity and density from WIND, the GOES-7 $E > 2$ MeV electron flux, the geostationary electron spectrum from Metosat-3/SEM-2 and corresponding McIlwain's L, the K_p planetary index and the D_{st} magnetic activity index.

Figure 2. For the same period as Figure 1, the 1.0–2.2 and 2.2–4.6 MeV outer-belt electron fluxes from Strv-1b/REM as a function of L, the D_{st} magnetic activity index, the Salammbô-3D results including the L-distribution of 600 keV equatorially mirroring electron flux, the energy spectrum at $L = 4$ of equatorially mirroring electrons and the α_0-distibution of 600 keV electron flux at $L = 4$, and the simulation of the Strv-1b/REM 1.0–2.2 MeV measurements from the Salammbô-3D results.

Figure 2. For the same period as Figure 1, the 1.0–2.2 and 2.2–4.6 MeV outer-belt electron fluxes from Strv-1b/REM as a function of L, the D_{st} magnetic activity index, the Salammbô-3D results including the L-distribution of 600 keV equatorially mirroring electron flux, the energy spectrum at $L = 4$ of equatorially mirroring electrons and the α_0-distibution of 600 keV electron flux at $L = 4$, and the simulation of the Strv-1b/REM 1.0–2.2 MeV measurements from the Salammbô-3D results.

Figure 3. Comparison of 1.0–2.2 MeV electron flux observed by Strv-1b/REM (thick green curves) with the Salammbô-3D simulation of these measurements (thin red curves) along four orbits: one before the storm, one during the main phase and two during the recovery phase.

Figure 3. Comparison of 1.0–2.2 MeV electron flux observed by Strv-1b/REM (thick green curves) with the Salammbô-3D simulation of these measurements (thin red curves) along four orbits: one before the storm, one during the main phase and two during the recovery phase.

Figure 4. Illustration of the energy increases for equatorially mirroring electrons due to a pure radial diffusion from $L = 7$. The different curves correspond to the energy range of the five Meteosat-3/SEM-2 energy channels.

Figure 4. Illustration of the energy increases for equatorially mirroring electrons due to a pure radial diffusion from $L = 7$. The different curves correspond to the energy range of the five Meteosat-3/SEM-2 energy channels.

Figure 5. Evaluation of McIlwain's L for Meteosat-3 (top panel) and Strv-1b satellites on 7 April 1995 using two different external magnetic field models: the *Olson and Pfitzer* [*1977*] quiet model (green curves) and the *Pfitzer and Olson* [*1988*] dynamic model (red curves).

Figure 5. Evaluation of McIlwain's L for Meteosat-3 (top panel) and Strv-1b satellites on 7 April 1995 using two different external magnetic field models: the *Olson and Pfitzer* [*1977*] quiet model (green curves) and the *Pfitzer and Olson* [*1988*] dynamic model (red curves).

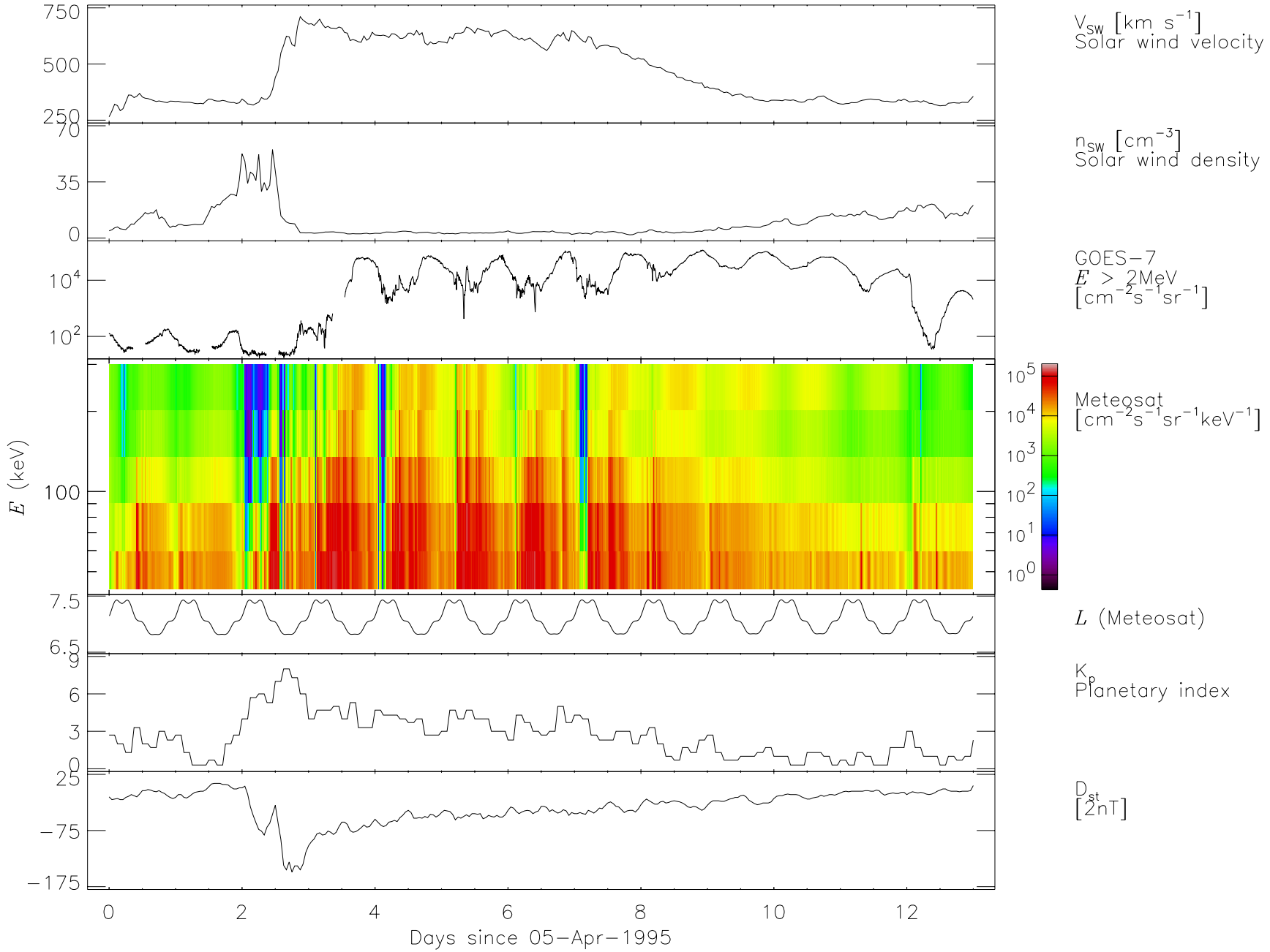
750
500
250
V_{SW} [km s^{-1}]
Solar wind velocity
70
35
0
n_{SW} [cm^{-3}]
Solar wind density
10^4
10^2
GOES−7
E > 2MeV
[$cm^{-2}s^{-1}sr^{-1}$]
E (keV)
100
10^5
10^4
10^3
10^2
10^1
10^0
Meteosat
[$cm^{-2}s^{-1}sr^{-1}keV^{-1}$]
7.5
6.5
L (Meteosat)
9
6
3
0
K_p
Planetary index
25
−75
−175
D_{st}
[2nT]
0
2
4
6
8
10
12
Days since 05−Apr−1995

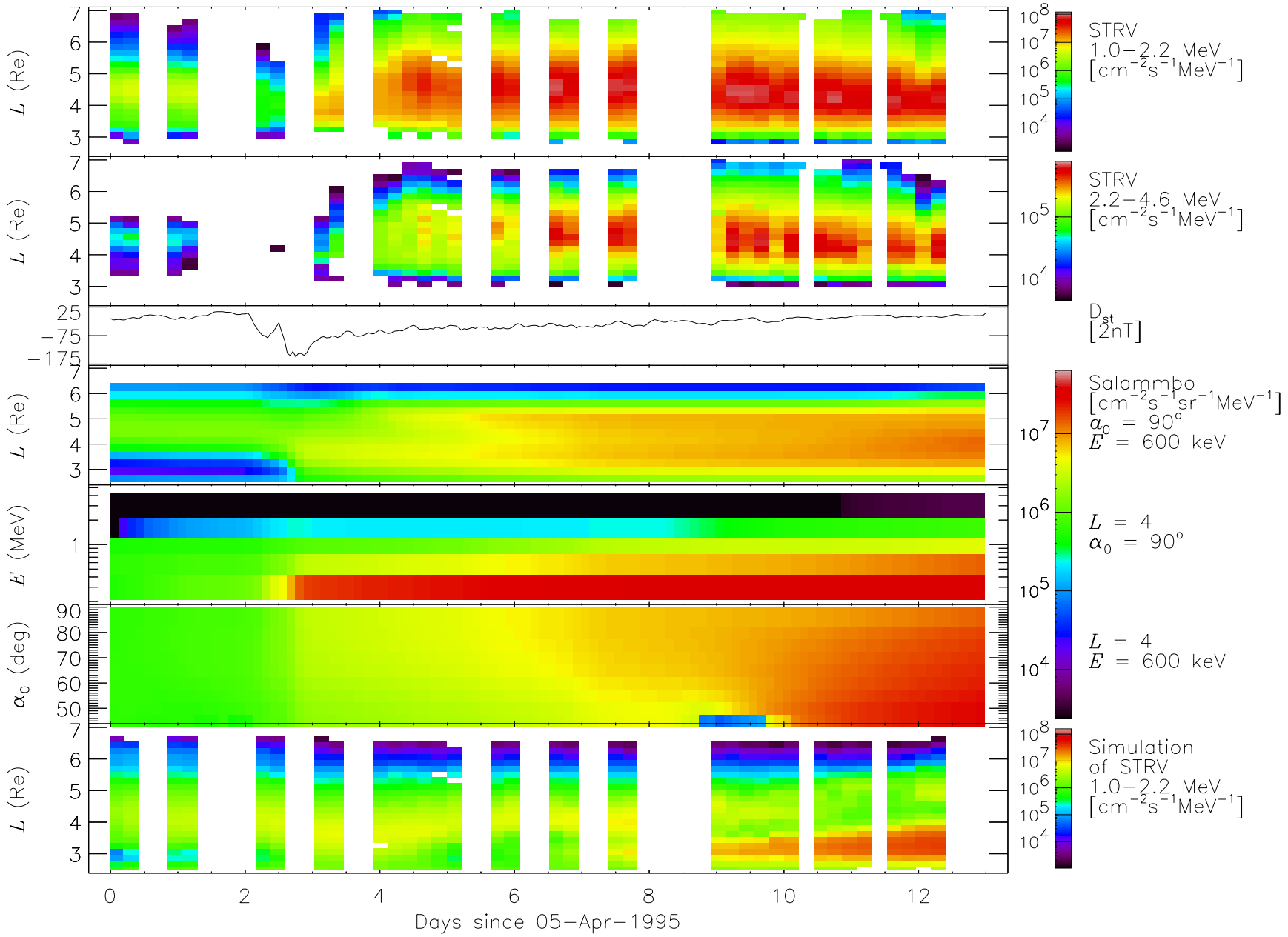
L (Re)
STRV
1.0−2.2 MeV
[cm⁻²s⁻¹MeV⁻¹]
STRV
2.2−4.6 MeV
[cm⁻²s⁻¹MeV⁻¹]
Dst
[2nT]
Salammbo
[cm⁻²s⁻¹sr⁻¹MeV⁻¹]
α0 = 90°
E = 600 keV
E (MeV)
L = 4
α0 = 90°
α0 (deg)
L = 4
E = 600 keV
Simulation
of STRV
1.0−2.2 MeV
[cm⁻²s⁻¹MeV⁻¹]
Days since 05−Apr−1995

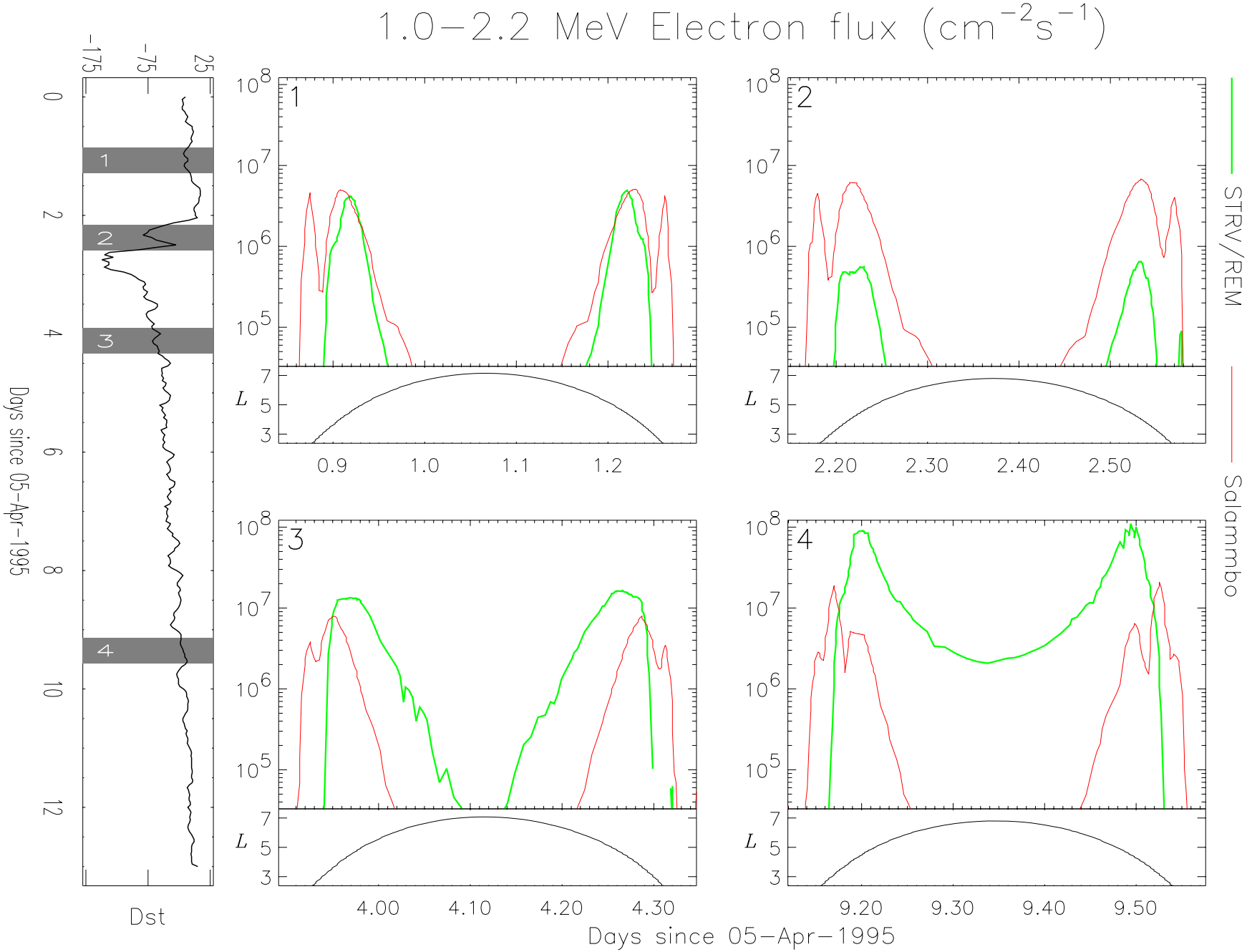
1.0−2.2 MeV Electron flux (cm^{-2}s^{-1})
Dst
−175
−75
25
Days since 05−Apr−1995
0
2
4
6
8
10
12
1
2
3
4
10^8
10^7
10^6
10^5
L
7
5
3
0.9
1.0
1.1
1.2
2.20
2.30
2.40
2.50
4.00
4.10
4.20
4.30
9.20
9.30
9.40
9.50
Days since 05−Apr−1995
STRV/REM
Salammbo

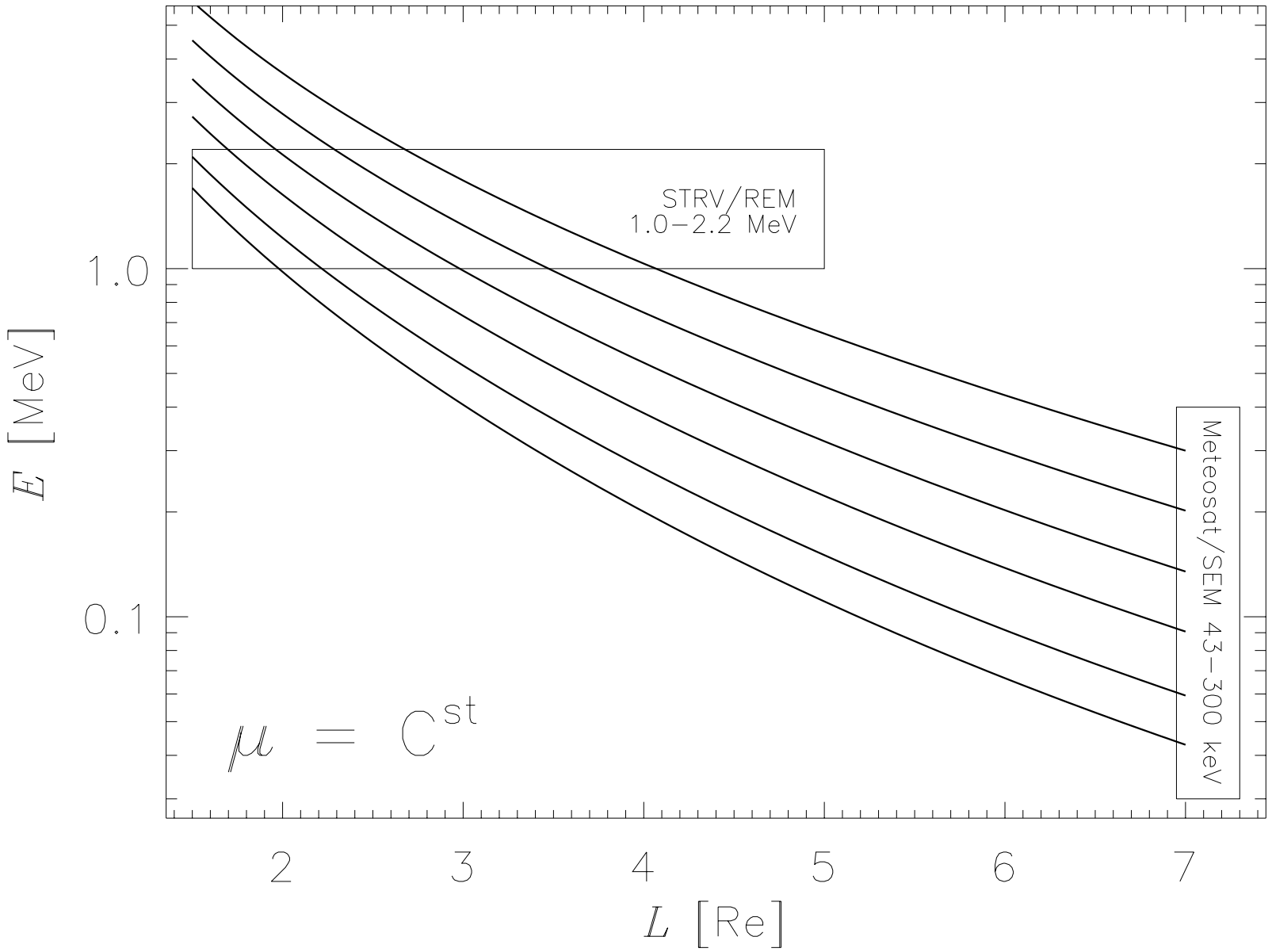
STRV/REM
1.0−2.2 MeV
Meteosat/SEM 43−300 keV
μ = C^st
E [MeV]
1.0
0.1
2
3
4
5
6
7
L [Re]

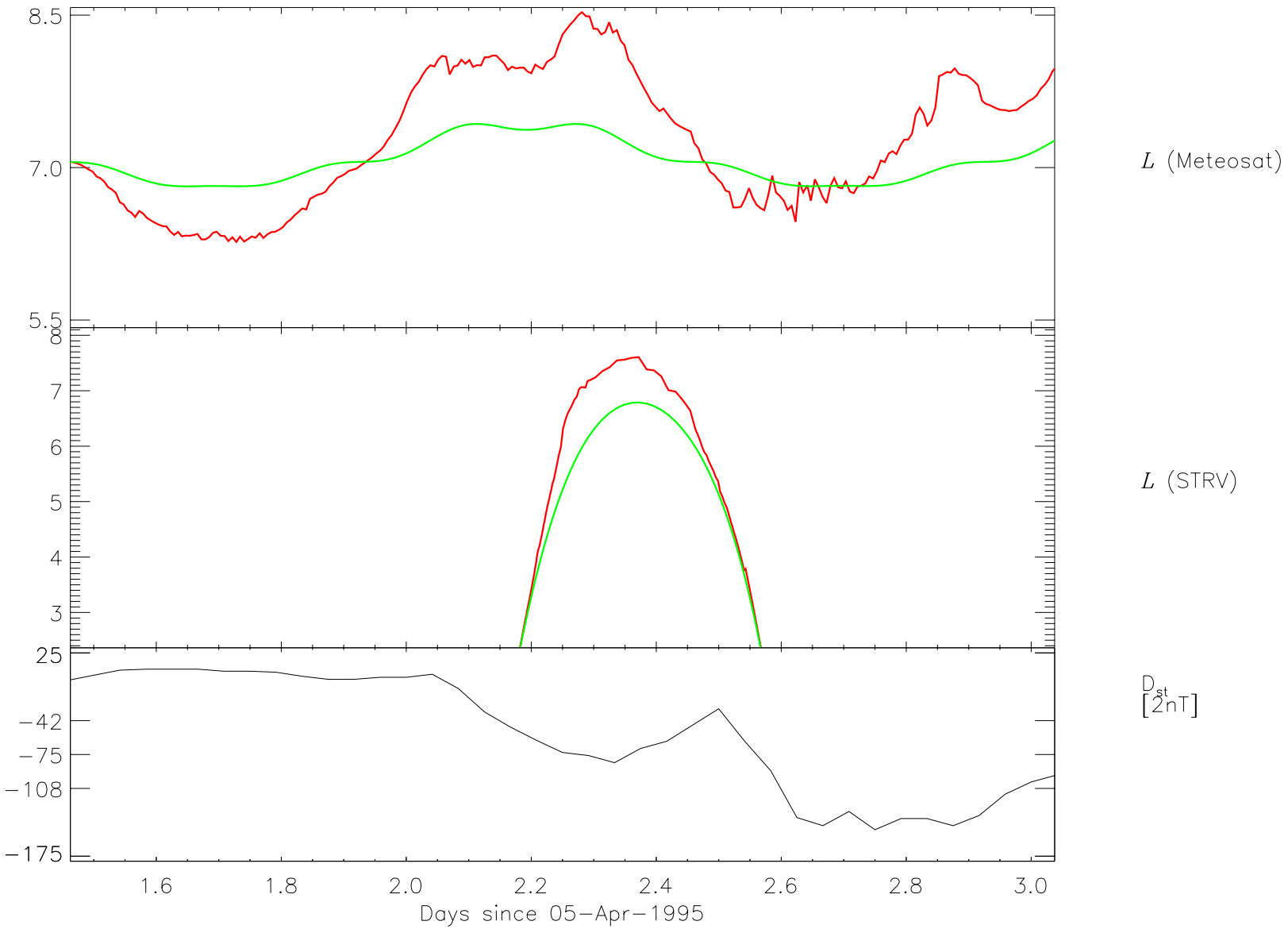
8.5
7.0
5.5
8
7
6
5
4
3
25
−42
−75
−108
−175
1.6
1.8
2.0
2.2
2.4
2.6
2.8
3.0
Days since 05−Apr−1995
L (Meteosat)
L (STRV)
D_st [2nT]